Northumbria Research Link

Signatures of quiet Sun reconnection events in Ca II, Hα, and Fe I

J. Shetye,[1,2]★ S. Shelyag,[3] A. L. Reid,[4] E. Scullion,[3] J. G. Doyle[2] and T. D. Arber[1]

[1]*Centre for Fusion, Space and Astrophysics, Department of Physics, University of Warwick, Coventry CV4 7AL, UK*
[2]*Armagh Observatory and Planetarium, College Hill, Armagh BT61 9DG, Northern Ireland, UK*
[3]*Department of Mathematics & Information Sciences, Northumbria University, Newcastle Upon Tyne NE1 8ST, UK*
[4]*Astrophysics Research Centre, School of Mathematics and Physics, Queen's University Belfast, Belfast BT7 1NN, UK*

ABSTRACT

We use observations of quiet Sun (QS) regions in the Hα 6563 Å, Ca II 8542 Å, and Fe I 6302 Å lines. We observe brightenings in the wings of the Hα and Ca II combined with observations of the interacting magnetic concentrations observed in the Stokes signals of Fe I. These brightenings are similar to Ellerman bombs (EBs), i.e. impulsive bursts in the wings of the Balmer lines that leave the line cores unaffected. Such enhancements suggest that these events have similar formation mechanisms to the classical EBs found in active regions, with the reduced intensity enhancements found in the QS regions due to a weaker feeding magnetic flux. The observations also show that the quiet Sun Ellerman bombs are formed at a higher height in the upper photosphere than the photospheric continuum level. Using simulations, we investigate the formation mechanism associated with the events and suggest that these events are driven by the interaction of magnetic field lines in the upper photospheric regions. The results of the simulation are in agreement with observations when comparing the light curves, and in most cases, we found that the peak in the Ca II 8542 Å wing occurred before the peak in Hα wing. Moreover, in some cases, the line profiles observed in Ca II are asymmetrical with a raised core profile. The source of heating in these events is shown by the MURaM simulations and is suggested to occur 430 km above the photosphere.

Key words: line: formation – line: profiles – Sun: chromosphere – Sun: photosphere.

1 INTRODUCTION

Ellerman Bombs (EBs) are prominent small-scale brightenings best observed in the far wings of Hα. They were first reported by Ellerman (1917) as hydrogen bombs and were termed EBs by McMath, Mohler & Dodson (1960), while Severny (1956) termed them moustaches. They appear with a flame-like morphology, are 1000–2000 km in length, and have vertical velocities of around 1 km s^{-1} with durations of 10–15 min (Zachariadis, Alissandrakis & Banos 1987; Georgoulis et al. 2002). EBs are generally observed near regions with relatively high concentrations of magnetic field, such as emerging flux regions and the penumbrae of sunspots (and references therein Isobe et al. 2007; Watanabe et al. 2008, 2011; Rutten et al. 2013; Vissers, Rouppe van der Voort & Rutten 2013; Nelson et al. 2015; Reid et al. 2016). Magnetic field configuration occurring in the photosphere dictates the morphology of the EBs (Georgoulis et al. 2002; Nelson et al. 2013b; Vissers et al. 2013; Reid et al. 2015; Reid et al. 2016; Tian et al. 2016). EBs are seen as enhanced intensities between 30 per cent and 55 per cent above average brightness in the wings of the Hα line profile, often present above the polarity

inversion line (Pariat et al. 2007; Watanabe et al. 2008; Reid et al. 2016).

EBs are also observed in other lines. Tian et al. (2016) observed EB-like events in Mn I 2795 Å, Mg II h & k lines, Ni II 1393.33 Å, and 1335.30 Å as enhancements in the wings rather than the core. EBs are observed in the Solar Dynamic Observatory's (SDO; Pesnell, Thompson & Chamberlin 2012) Atmospheric Imaging Assembly (AIA, Lemen et al. 2012) 1700 channel as small brightenings. Of the 10 events that Tian et al. (2016) identified as ultraviolet (UV) bursts (Peter et al. 2014; Vissers et al. 2015), seven were along the magnetic inversion line, and three were co-spatial with EBs. Qiu et al. (2000) show that there is a significant correlation with EBs in the Hα wings at ± 1.3 Å and the UV continuum at 1600 Å. Fang et al. (2006) and Pariat et al. (2007) noted the presence of EBs in the Ca II 8542 Å lines. Spectropolarimetric observations done by Pariat et al. (2007) show that EBs are formed when opposite polarities merge giving rise to a cancellation of magnetic flux. As this cancellation occurs, plasma is heated and accelerated deep in the atmosphere, and this is seen as a double-shaped hump in IRIS Si IV, C II, and Mg II lines. The total energies needed to produce EBs are estimated to be in the range of 10^{27}–10^{28} erg (and references therein Georgoulis et al. 2002), however, in the IRIS observations, the energy needed

★ E-mail: j.shetye@warwick.ac.uk

to drive the UV bursts is of the order of 10^{29} erg (Peter et al. 2014). Rouppe van der Voort, Rutten & Vissers (2016) studied EB-like brightenings in the quiet Sun (QS) and suggested that these EBs can only be identified at the telescope's diffraction limit of $\lambda/D = 0.14$ arcsec at 6563 Å in SST data at a much lower intensity change, thus relaxing the 50 per cent above average intensity requirement usually used to define EBs. Such QS observations of EBs were also reported by Nelson et al. (2017). Reid et al. (2017) report micro-flaring events that are in some cases similar to the classical definition of EBs and discussed the need for redefining EBs, based on signatures depending only on observations.

1.1 Magnetic concentrations and pseudo-EBs

Vissers et al. (2013) classify an EB when the mean-intensity enhancements are between 30 per cent and 55 per cent in the Hα line wings, compared to the average background line profiles. They further show that the bright grains, which are found simultaneously in the Ca II H, and the G-band images are bright network points. Such bright network points are driven by strong magnetic field concentrations (Sheeley 1969; Vrabec 1971; Harvey & Harvey 1973; Muller & Mena 1987; Hagenaar & Shine 2005).

Spruit (1976) suggests that these magnetic concentrations (MCs) are bright in the continuum of hot-wall radiation. Berger et al. (2004) and Rouppe van der Voort et al. (2005) indicate that the MCs rapidly evolve with complex morphologies. However, the MCs are found in the dark intergranular lanes and are only observed at a sub-arcsecond resolution (Title & Berger 1996). MCs are further observed in Mn I (Livingston & Wallace 1987), line wings of Hα (Leenaarts et al. 2006), and the G-band (Leenaarts et al. 2006). They are less sharp in the Ca II H. In the Dutch Open Telescope (DOT) movies, Rutten et al. (2013) report that MCs appear in the blue wing of Hα, suggesting down flows. On comparing the signatures in Hα and Na I D, they see MC shocks accompanied with blue-wing enhancements in Hα.

Furthermore, Rutten et al. (2013) suggested that the mean intensity change in the wings of the Hα line has to be at least 50 per cent with respect to the average background line profile, and all EBs fainter than this should be considered as pseudo-EBs irrespective of the formation mechanisms. Such a definition suggests that the 3500+ EBs studied by Nelson et al. (2013b) are pseudo-EBs. Additionally, Vissers et al. (2015) suggested that the false positives by Nelson et al. (2013b) are because the regions studied were close to a decaying sunspot, rather than an emerging sunspot. The most important difference between an MC and an EB is that EBs are related to reconnection.

1.2 Quiet Sun EBs

Quiet Sun Ellerman bombs (QSEBs) have a similar topology to EBs, such as a bright flame and lifetimes of a few minutes. Rouppe van der Voort et al. (2016) observed these events in the Hα, Fe I 6173 Å, and Ca II 8542 Å wavelengths, in combination with IRIS and AIA/SDO. They found the EB intensities significantly lower than the active region EBs. However, the authors suggest that these EBs are also consequences of reconnection. Moreover, they also suggested that QSEBs are detected only when the data are of a high quality. Such data can be acquired from the SST (Scharmer et al. 2003) and are enhanced with the support of the adaptive optic system and image-reconstruction techniques such as Multi-Object Multi-Frame Blind Deconvolution (MOMFBD, van Noort, Rouppe van der Voort & Löfdahl 2005). Rouppe van der Voort et al.

(2016) identify 24 QSEBs in a 2013 July 4 09:20 UT data set and a further 21 QSEBs in a 2013 July 4 10:13 UT data set. Furthermore, they describe QSEBs to have lengths between 150 and 360 km and widths ≈ 170 km. QSEBS are observed in positions H$\alpha \pm 1.3$ Å and last for a few minutes. QSEBs tend to have a predominantly bipolar topology, where after reconnection, both polarities seem to diminish. The intensity enhancement was below 40 per cent in the Hα line wing (in relation to the reference spectrum). Also, they concluded that these QSEBs are not observed in Ca II as they could not find significant evidence. In addition, Nelson et al. (2017) show the presence of QSEBs in their data set.

1.3 Layout

We show certain cases of enhancements in the wings of Hα, in the range of 10–20 per cent (above the QS average intensity) associated with the interaction of opposite polarities observed in Fe I. Most of these events are also observed in Ca II line wings with some events showing core enhancement. Such Ca II line wings enhancements were not reported with QSEBs before. We use the light curves in Hα, Ca II, Stokes-V, and Stokes-I from Fe I to investigate the evolution of QSEBs. Using a time series of magnetized photospheric models produced by the MURaM simulations (Vögler et al. 2005), we further analyse the character of plasma motions in intergranular magnetic field concentrations and in particular the formation height as seen in Hα and Ca II 8542 Å. Such an approach provides a comprehensive understanding of the source of heating associated with these QSEBs.

The rest of the paper is organized as follows: Section 2 and Section 3, describe the methodology used in the project. Section 4 discusses the analysis with two detailed case studies. The simulation aspect is described in Section 5. The conclusions and key points from the paper are summarized in Section 6.

2 OBSERVATIONS

We investigate a QS disc centre dataset, taken between 08:07:24 and 09:05:46 UT on 2012 June 21 using CRisp spectro-polarimeter (CRISP; Scharmer et al. 2008) on the Swedish 1-m Solar Telescope (SST; Scharmer et al. 2003). We use QS observations in Hα (6563 Å), Ca II (8542 Å), and Fe I (6302 Å). The field-of-view (FOV) was centred in the QS at $[-3.1$ arcsec, 69.9 arcsec]. Fig. 1 shows the location of the FOV against AIA 1700 Å channels. The panels show the zoomed-in view of SDO AIA 1600 and 1700 Å channels, with corresponding Hα (6563 Å), Ca II (8542 Å) images. Crosses (X) represent the locations of 10 selected events, and A corresponds to a unipolar event. MOMFBD data reduction was performed using the method by van Noort et al. (2005). In the Hα wavelength, we observed at 10 line positions corresponding to ± 1.29, ± 1.03, ± 0.774, ± 0.516, and ± 0.258 Å from the line centre at 6563 Å (corresponding to Doppler velocities of ± 59, 47, 35, 23, and 12 km s^{-1}. In Ca II (8542 Å), we observe at ± 0.495, ± 0.440, ± 0.384, ± 0.330, ± 0.275, ± 0.219, ± 0.165, ± 0.110, and ± 0.054 Å with respect to the line centre at 8542 Å. In Fe I (6302 Å), we obtained spectro-polarimetric observations only at one position at about -40 mÅ from the line core. The cadence of this data set is 8s.

3 DETECTION METHOD

We use the EB detection automation code 'EBDATA' by Reid et al. (2016). The algorithm can detect and track MCs. The algorithm
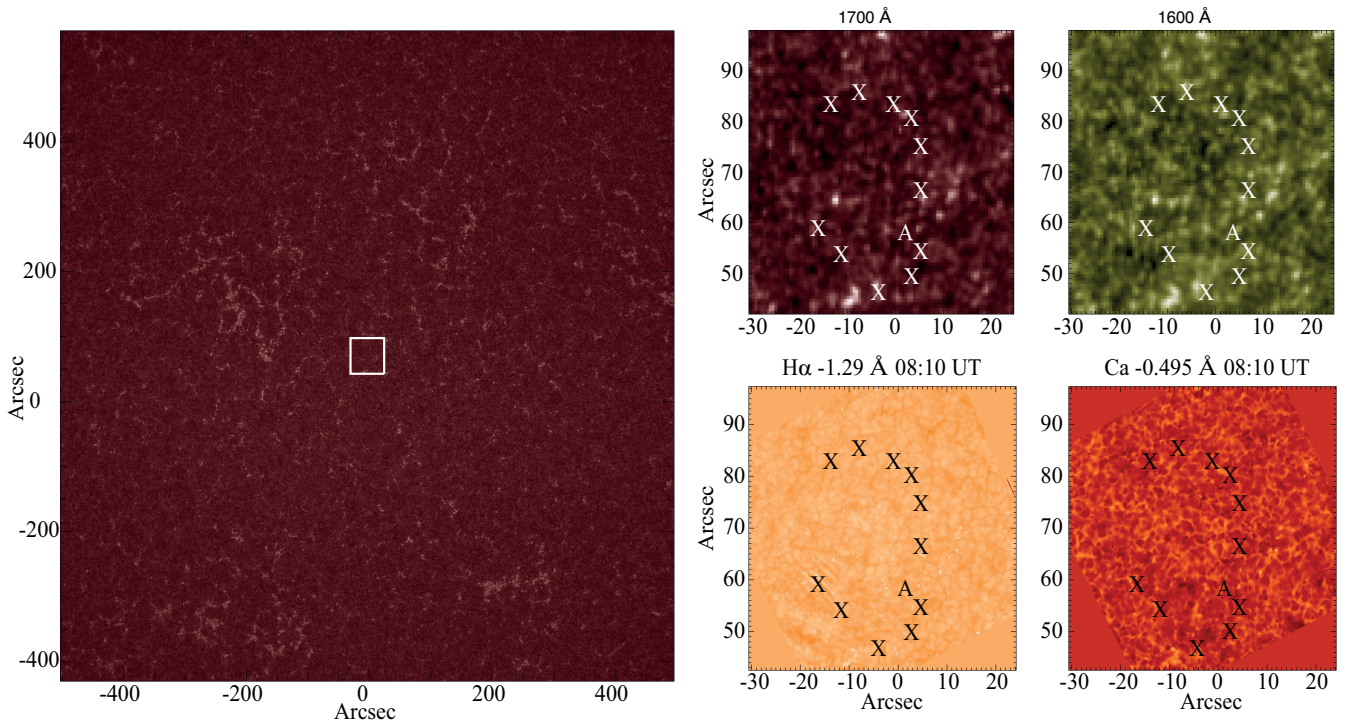
Figure 1. The QS region observed using CRISP on SST. The left-hand panel shows the location of the QS SST FOV overplotted against the AIA 1700 Å channel. The panels on the right-hand side show the zoomed-in view of the SDO AIA 1600 and 1700 Å channels, with corresponding Hα (6563 Å), Caɪɪ (8542 Å) images obtained from SST. Crosses (X) represent the locations of 10 selected events, and A corresponds to a unipolar event.

relies on parameters of the MCs, such as intensity threshold, area, size, and lifetime. The detection code also compares changes in intensity of the events with respect to surrounding intensity changes. In order to allow detections in the QS regions with low-intensity changes (compared to the background), we made minor changes to the algorithm. We define an event as a QSEB when the intensity contrasts, calculated in the Hα wings, for at least one pixel is 10 per cent more than the background average intensity. QSEBs evolve in time. This evolution is in terms of lateral motion as well as growth in size. The intensity of the grown area has to be greater than 10 per cent of the background average intensity, in both wings of the Hα at ±1.29 Å. The area of the QSEB, when it is fully grown has to be greater than 2 pixels (132 km). The line core in Hα must remain unchanged (no more than 1 per cent increase to account for variability as per Reid et al. 2016). We detected 334 events that are summarized in Fig. 2. The left-hand panel of Fig. 2 shows a relation between the fractional change in the Hα wing intensity and the apparent flux represented by the Stokes-*V* amplitude. The right-hand panel shows a relation between the fractional change in the Hα wing intensity and the rate of change of Stokes-*V* amplitude. Here, the maximum intensity is given as the maximum value in the wings of the detected pixels relative to the FOV average. The rate of change of Stokes-*V* amplitude is computed from change of Stokes-*V* amplitude throughout the lifetime of the events. Most of the events identified by the routine were unipolar MCs, shown by red circles and blue stars in the left-hand panel of Fig. 2. The rest were bipolar MCs with possible EB-like wing enhancements. These are represented by black crosses in the left-hand panel of Fig. 2. The events with less than 50 units of Stokes-*V* signal are termed as weak events and are represented by green squares in the left-hand panel of Fig. 2. In addition, the automated procedure also detected some long-lasting events with a strong unipolar field,

which would lie on the right-hand side of the left-hand panel of Fig. 2 between Stokes-*V* amplitude of '1000 and 1500'. These unipolar events would correspond to a very low change in Stokes-*V* signal and would lie near the '0' mark in the right-hand panel. The right-hand panel of Fig. 2 shows events, which showed flux cancellation on the left-hand side, with negative flux signs. The events that showed emergence of flux are represented on the right-hand side of the plot, these show positive flux. All the selected events show flux cancellation.

We manually selected 10 events from the detected events shown in Fig. 2 satisfying properties of active region EBs, where magnetic flux cancellations are accompanied with wing enhancements in Hα and Caɪɪ 8542 Å. The events shown here are further selected by manual detection that focused on (1) interaction of QSEBs in Feɪ 6302 Å Stokes-*V* wavelength, (2) sudden intensity enhancements in the Hα wing positions, and (3) sudden intensity enhancements in the Caɪɪ 8542 Å wing positions. These intensity enhancements are smaller compared to regular active region EBs. After detecting events using the code, we manually checked whether they were formed above the interacting opposite polarity regions. Fig. 2 shows scatter plots highlighting the comparison between properties of all detections and selected events. These events are labelled by the numbers 1–10 in Fig. 2. For the selected events we present the snapshots of the Hα wing position at −1.29 Å, Caɪɪ 8542 Å at −0.495 Å, and Feɪ 6302 Å Stokes-*V* as well as their appearance in the SDO AIA's 1600 and 1700 Å wavelengths in Fig. 3. The white and black boxes are overplotted on the images. These boxes represent the region of interest, which are then used for further analysis. Three of the selected events have recurring intensity enhancements. Such EB recurrence have also been seen in active regions (Qiu et al. 2000; Nelson et al. 2015; Reid et al. 2016).
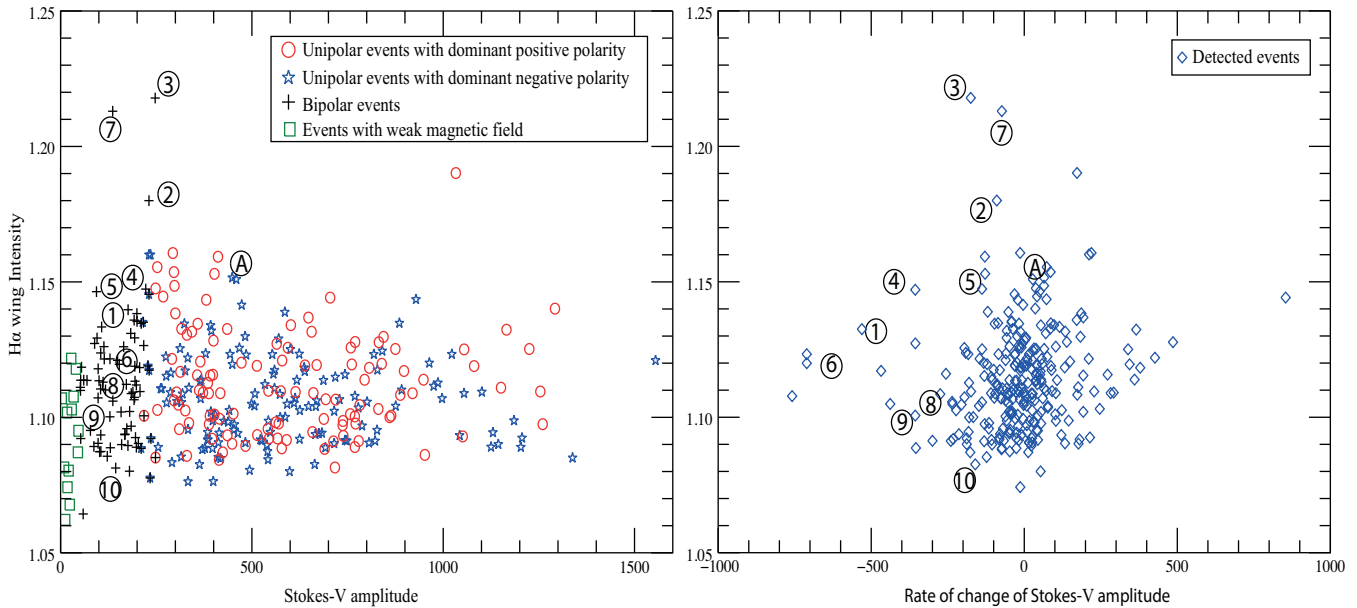
Figure 2. Scatterplot of detected events represented as follows: In the left-hand panel, a relation between fractional change in the Hα wing intensity and the Stokes-*V* amplitude, and in the right-hand panel, the relationship between the fractional change in the Hα wing intensity and the rate of change of the Stokes-*V* signal. In the left-hand panel, the unipolar regions are represented by the red circles and the blue stars. Bipolar regions are represented by black plusses. The events with less than 50 units of Stokes-*V* signal (weak events) are represented by the green squares. The manually selected regions are represented by numbers 1–10, and 'A' represents a sample unipolar event. In the right-hand panel, all the events are represented by the blue diamonds with the selected events represented by 1–10 with a sample unipolar region represented as 'A' (see text for details).

4 ANALYSIS AND RESULTS

Fig. 2 shows the manually selected events labelled 1–10. In the left-hand panel of Fig. 2, the selected events lie in the region of bipolar detections with Hα wing intensities between 1.06 and 1.23 and a high reduction in the Stokes-*V* intensity. A unipolar scenario event identified by the detection algorithm is labelled 'A' in the plot. This event is not considered as a QSEB. This event shows maximum intensity similar to some bipolar detections, however, since the event does not evolve during its lifetime, the rate of change of Stokes-*V* intensity is nearly zero. The same goes with other events identified by the detection code. The manually selected events are bipolar MCs with a significant reduction in the Stokes-*V* intensity. Thus, the manually selected events stand out and have different properties from the other unipolar/bipolar events.

4.1 Light curves

In column 1 of Figs 4 and 5, we plot Hα (solid black) and CaII 8542 Å (black dashed) light curves. The Hα light curves are computed at ±1.29 Å, and the CaII 8542 Å light curves are computed at ±0.495 Å. We plot the light curves for the selected events by taking all pixels relating to the feature and summing the intensities in the blue and the red wing of the Hα and CaII 8542 Å lines. The output is then divided by an average value. The light curves show an impulsivity corresponding to EB-like line wing enhancements. We see enhancements in the Hα and CaII 8542 Å wings. The minimum intensities of the light curves correspond to times where the Hα intensity contrast came back to the averaged background intensity. The maximum intensities correspond to our events observed in the Hα and CaII 8542 Å wing. We plot the light curves in Stokes-*V* (solid black) and Stokes-*I* (black dashed) signal at −40 mÅ from the Fe 6302 Å line centre. The light curves are shown in column 2 (middle column). The light curves are plotted in black solid and dashed

colours, respectively, in Figs 4 and 5. We see that as one polarity disappears, the net flux also reduces, indicating a cancellation of the magnetic field. In the column 3 of Figs 4 and 5, we plot the light curves corresponding to the SDO–AIA channels 1600 Å (solid black) and 1700 Å (black dashed). These are plotted by averaging all pixels corresponding to the events and dividing by the maximum intensity. These light curves represent the AIA 1600 and 1700 Å channels before and after the events. The green dotted vertical lines show the locations of the events as observed in CRISP.

From Figs 4 and 5, we see that in most cases (9 of 10) the peak in intensity light curves occurs in the wings of CaII 8542 Å before Hα. The offsets at these positions are shown in Table 1. We can calculate the velocity of the down flow of the intensity enhancement. The approximate heights between the formation of Hα and CaII 8542 Å are assumed to be 500 km from models by Leenaarts et al. (2009) and Leenaarts, Carlsson & Rouppe van der Voort (2012). The propagation speed of the enhancements is approximately calculated using (distance/time) as 6 km s^{-1}. For the EBs showing recurring activity, these velocities are calculated using the difference between most prominent peaks in the light curves of Hα and CaII 8542 Å. The impulsive nature of the events is associated with a corresponding decrease in the Stokes signals, thus suggesting that the intensity enhancements correspond to the magnetic flux cancellation possibility mentioned in Georgoulis et al. (2002). Comparing the 1600 and 1700 Å light curves with the Hα and CaII 8542 Å, the intensity peaks observed in 1600 and 1700 Å occur after the main intensity peaks observed in the Hα and CaII 8542 Å (see cases 1, 3, 4, and 5). In some cases, there is no apparent signature in the SDO channels (see case 6, 7, and 9). There are some cases that show a brightening in SDO–AIA channels at the location of the event. This brightening lasts for only one SDO frame (cases 2, 8, and 10). It is not clear whether these brightenings correspond to the event as it often appears after a delay. In addition, the light curves
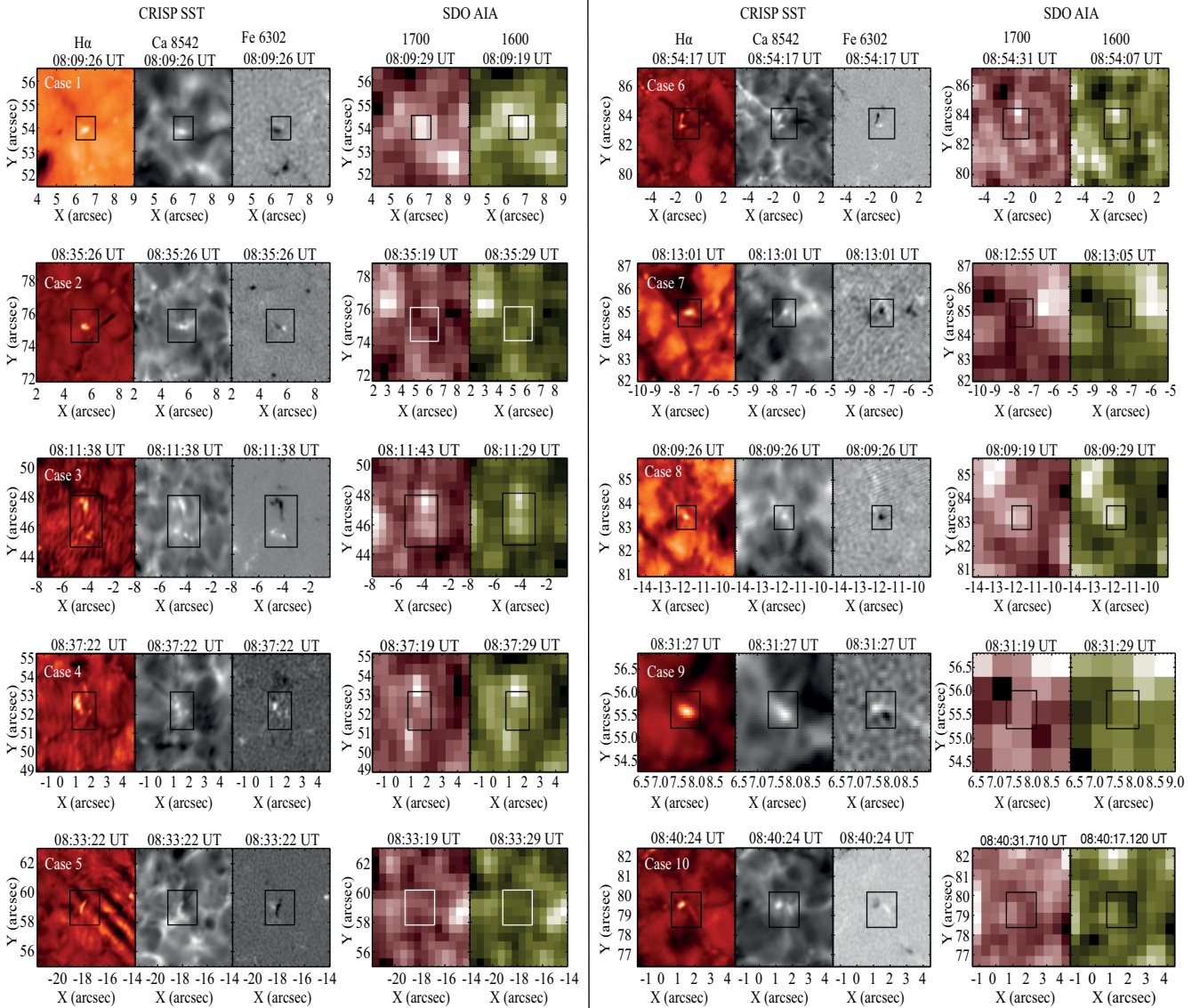
Figure 3. Snapshots of 10 possible QSEBs. The panels show the event in Hα (first column) wing position −1.29 Å, CaII 8542 Å wing position −0.495 Å(second column), and FeI 6302 Å Stokes-*V* (third column). The AIA data from 1600 to 1700 Å are shown in the fourth and fifth columns, respectively. The boxes overplotted on the images show the location of the QSEBs.

of cases 3, 8, and 10 in Figs 4 and 5 show multiple impulsive bursts. Such behaviour is analogous to EBs observed near a large source of magnetic flux. The light curves show that the QSEBs presented here form at an atmospheric level a few hundred kilometres above the photospheric continuum. This is shown by the different timings of the peak intensity between CaII 8542 Å and Hα light curves.

4.2 Categories

By obtaining observations across multiple wavelengths, we can correlate the physics involved in events such as EBs. In Fig. 3, we show snapshots of 10 cases. The snapshots are taken at the Hα wing position −1.29 Å, CaII 8542 Å wing position −0.495 Å, and FeI 6302 Å Stokes-*V*. The boxes represent the region-of-interest (ROI). Based on the observations, events can be categorized in the following evolutionary characteristics: (1) Single impulsive events involving reduction in Stokes-*V* after the intensity peaks in Hα and CaII 8542 Å wings as in the light curves for cases 1, 2, 7, and 9. In

case 9, the CaII 8542 Å and Fe I 6302 Å Stokes-*V* track each other more closely than Hα, which is a common observational effect of dynamics related to MCs. However, this reduction in intensity is followed by interaction of opposite polarity MCs that gives rise to impulsivity. (2) Events associated with reduction in Stokes-*V* signal where the two polarities keep on interacting (cases 3, 8, and 10). This reduction is observed with a repetitive impulsive nature in the Hα and CaII 8542 Å wings, during the time of the interactions. The presence of Ca II 8542 Å wing emissions in addition to Hα emissions in all the cases suggests that such events are triggered in the lower chromosphere. The events studied show lifetimes of ~800 s with intensity change of <10 per cent in comparison to the average spectral lines. The velocity corresponding to the lateral motion of the selected events lies in the range of 0.3–2.4 km s^{-1}. This velocity is computed by 'EBDATA' detection algorithm. This velocity range matches with EBs found near active regions (Zachariadis et al. 1987).
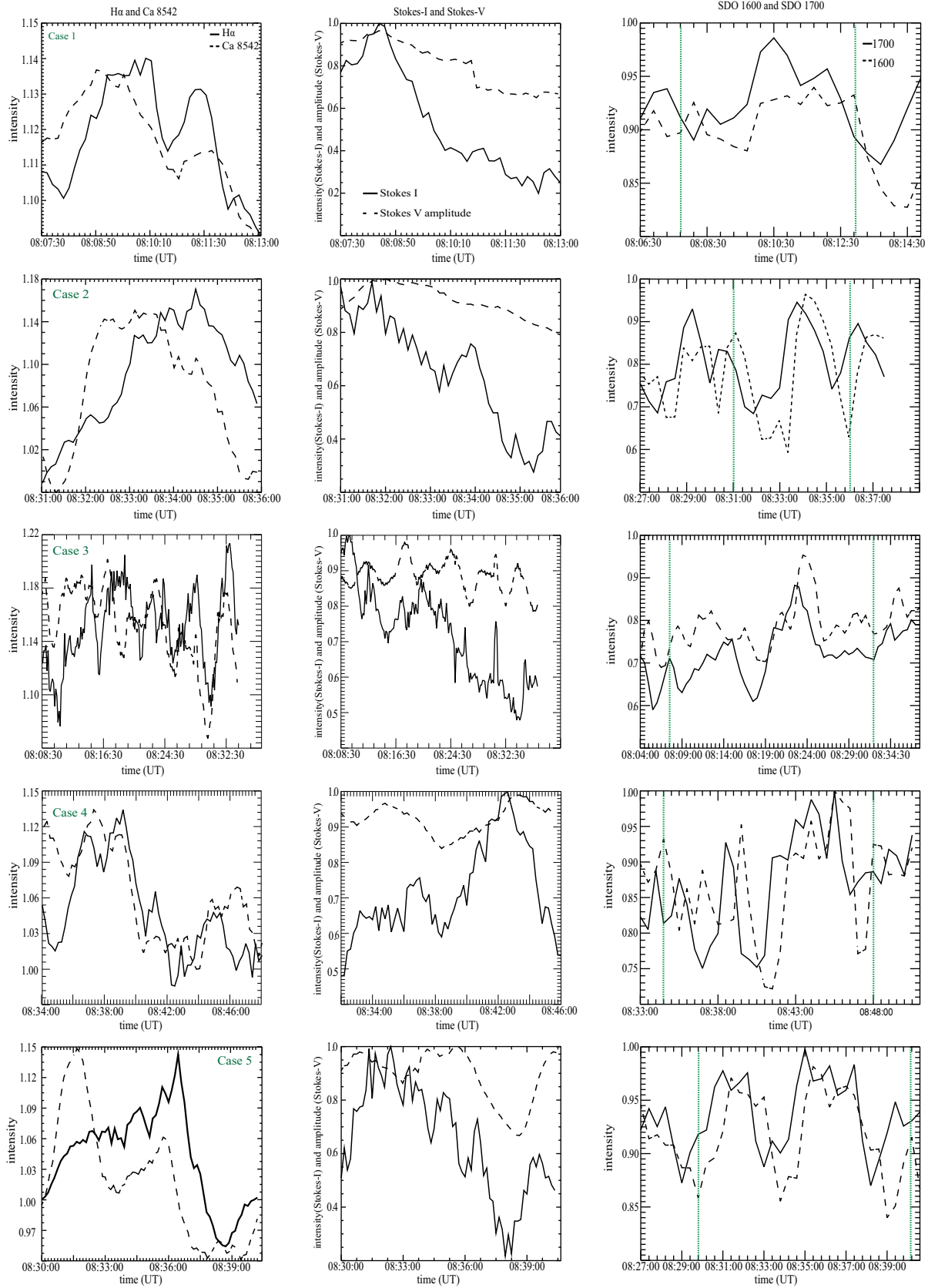
Figure 4. The light curves for cases 1–5. Column 1: The light curves in Hα (solid black) wings at ± 1.29 Å and CaII 8542 Å (black dashed) wings at ± 0.495 Å. Column 2: The light curves representing amplitude of FeI 6302 Å Stokes-*V* (black dashed) and Fe I 6302 Å Stokes-*I* (solid black). Column 3: The light curves in 1600 (solid black) and 1700 Å (black dashed) channels obtained from SDO–AIA. The vertical green dotted lines overplotted on the light curves obtained in the 1600 and 1700 Å channels represent the start time and end time of the event as observed in Hα (solid black) and CaII.
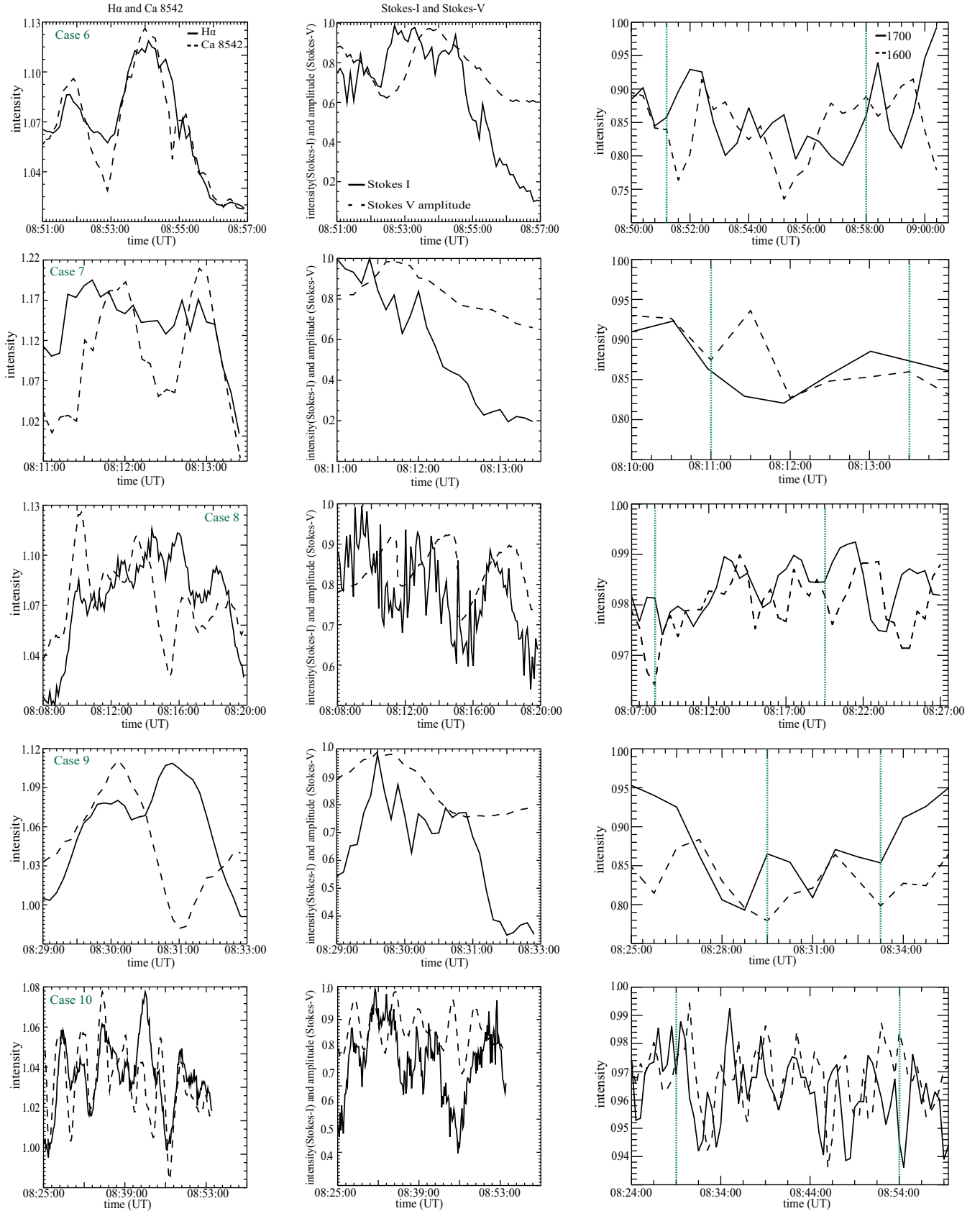
Figure 5. The light curves for cases 6–10. Column 1: The light curves in Hα (solid black) wings at ± 1.29 Å and CaII 8542 Å (black dashed) wings at ± 0.495 Å. Column 2: The light curves representing amplitude of FeI 6302 Å Stokes-*V* (black dashed) and Fe I 6302 Å Stokes-*I* (solid black). Column 3: The light curves in 1600 (solid black) and 1700 Å (black dashed) channels obtained from SDO–AIA. The vertical green dotted lines overplotted on the light curves obtained in the 1600 and 1700 Å channels represent the start time and end time of the event as observed in Hα (solid black) and CaII.

Table 1. Calculation of plasma velocity.

Case No	ΔT s	Velocity of plasma. (Km s^{-1})
1	60	8.33
2	120	4.15
3	**420**	**1.21**
4	80	6.25
5	260	1.92
6	10	50
7	**-30**	**+16.4**
8	**300**	**1.51**
9	640	0.78
10	**330**	**1.51**

4.3 QSEB morphology

In Fig. 6, we show a small EB-like event. In the top-most row with panels A1–A4, we see that the two polarities interact continuously in the Fe I Stokes-V evolution. Such interaction gives rise to an enhanced emission in the Hα wing images taken at ± 1.29 Å and Ca II 8542 Å line profile at ± 0.495 Å. The panels B1–B4 and D1–D4 of Fig. 6 show snapshots taken in the Hα wing position −1.29 Å and Ca II 8542 Å wing positions at −0.495 Å. We see typical EB topologies in both Hα and Ca II 8542 Å images (see arrows in Fig. 6). In panels C1–C4 and E1–E4 of Fig. 6, we show snapshots of the line profiles with dashed green lines against background line profiles (the background line profile is the average background across the FOV) shown in the solid black lines. We see that there is a contrast change between 10 per cent and 20 per cent while comparing to the average Hα spectrum. In Ca II 8542 Å, we see that such events have higher contrast changes from 20 per cent to 40 per cent compared to the average Ca II 8542 Å spectrum. However, the line profile in Ca II 8542 Å is asymmetric, see panel E3 of Fig. 6.

In Fig. 7, we show an event that involves two MCs interacting for ∼15 min. The photospheric flux cancellation is followed by repetitive emissions in the Hα and Ca II wings. In the panels A1–A4, we see opposite polarities interacting in the Fe I 6302 Å line core images, in the evolution. The interaction between negative and positive polarity causes the weaker polarity to be annihilated over the evolution (not shown here). Furthermore, the panels A1–A4 show evolution of the two polarities, where the positive polarity is seen to diminish in size in panel A4 compared to A1. This merging and interaction gives rise to multiple intensity peaks, seen in the Hα wing position −1.29 Å and Ca II 8542 Å −0.495 Å images (see panels B1–B4 and D1–D4). Below both Hα and Ca II 8542 Å images, we show snapshots representing line profiles with dashed green lines against solid black lines that represent the average background spectrum (see panels C1–C4 and E1–E4).

4.4 A sample unipolar event

The EBDATA algorithm detected 334 events, of which 10 were selected for detailed analysis. We discuss here the evolution of a unipolar event that was discarded as a 'false positive'. The unipolar event is labelled 'A' in the Fig. 2. The snapshots of the evolution of this unipolar event are shown in panels A1–A3 of Fig. 8 with larger negative polarity seen in the Fe I 6302 Å Stokes-V. We see that the two unipolar flux regions interact with each other combining to form bigger negative polarity in size (sub panels A1–A3 of

Fig. 8). In panels B1–B3, we show a series of the Hα images. We see enhancements in the intensity at locations where the unipolar flux region combines. Such intensity enhancements are also seen in panels D1–D4. In both the Hα and Ca II images, we see EB-like wing enhancements. The Hα and Ca II 8542 Å line profiles show a similar behaviour of emission compared to previous examples (see the snapshots of line profiles seen in panels C1–C3 and E1–E3, respectively). However, Ca II 8542 Å line profile shows a strong blue-shifted line profile with core enhancements. Such events could be due to shearing reconnection, low-resolution imaging fails to spot the opposite polarity, or they could be driven by braided reconnection. Furthermore, Fig. 9 shows no clear relation between the Hα (solid black) and Ca II 8542 Å (black dashed) light curves. The examples here show impulsivity observed in Hα, which may or may not be related to the QSEBs. Hence, we have ignored such detections.

The observational diagnosis indicates that in disc-centre viewing along the radial direction, only the top of an EB is seen, which shields what lies underneath as noted in simulations by Danilovic (2017). Thus, there is an absence of flame-like topology here. Also, in comparison with the 1600 and 1700 Å channels, we see no particular correspondence with the EB signatures observed in Hα and Ca II 8542 Å. However, we do note that in some cases there is some brightening that occurs after the initial EB brightening that could be related to these events. A possible explanation for the lack of UV enhancement could be due to the lower spatial resolution of the SDO–AIA instrument, or the lower height at which the UV continua form. It is analogous to reports by Rouppe van der Voort et al. (2016). Danilovic (2017) concludes that the strongest brightening corresponds to a significant temperature and density increase that occur at the site of the cancellation of two magnetic features of opposite polarities. Furthermore, the authors also highlight that unipolar regions are also strong EB candidates when accompanied by flux cancellation. This highlights that many detected unipolar regions could be an EB candidate. Georgoulis et al. (2002) suggest that flux cancellation is possible in unipolar regions by shearing reconnection. Furthermore, Hansteen et al. (2017) using BiFROST simulations suggest a weak brightening in Si IV associated with EBs.

5 MURAM SIMULATIONS

The aim of this simulation is to understand the formation mechanisms related to QSEBs. They complement the observations as the simulations performed in MURaM (Vögler et al. 2005) tell us where these events are formed. The code is used to perform simulations of the interaction of the magnetic field concentrations in the solar photosphere. This particular setup is for a QS region. The numerical setup for these set of observations is similar to the one described in Nelson et al. (2013a). The spatial resolution of the box is 25 km × 14 km × 25 km. The temporal resolution of the simulation is 50 s. A positive–negative 'checkerboard' vertically directed magnetic field, with the unsigned strength of 200 G is added to a well-developed non-magnetic photospheric convection snapshot. Then, the computational domain is set to evolve for a small number (2–5) of granular lifetimes. During the evolutionary period, most of the magnetic field cancels out, leaving some substantial magnetic field concentrations of opposite polarities in the intergranular lanes of the simulated photospheric granulation. These magnetic field concentrations move along the intergranular lanes occasionally coming in proximity to each other and reconnecting.
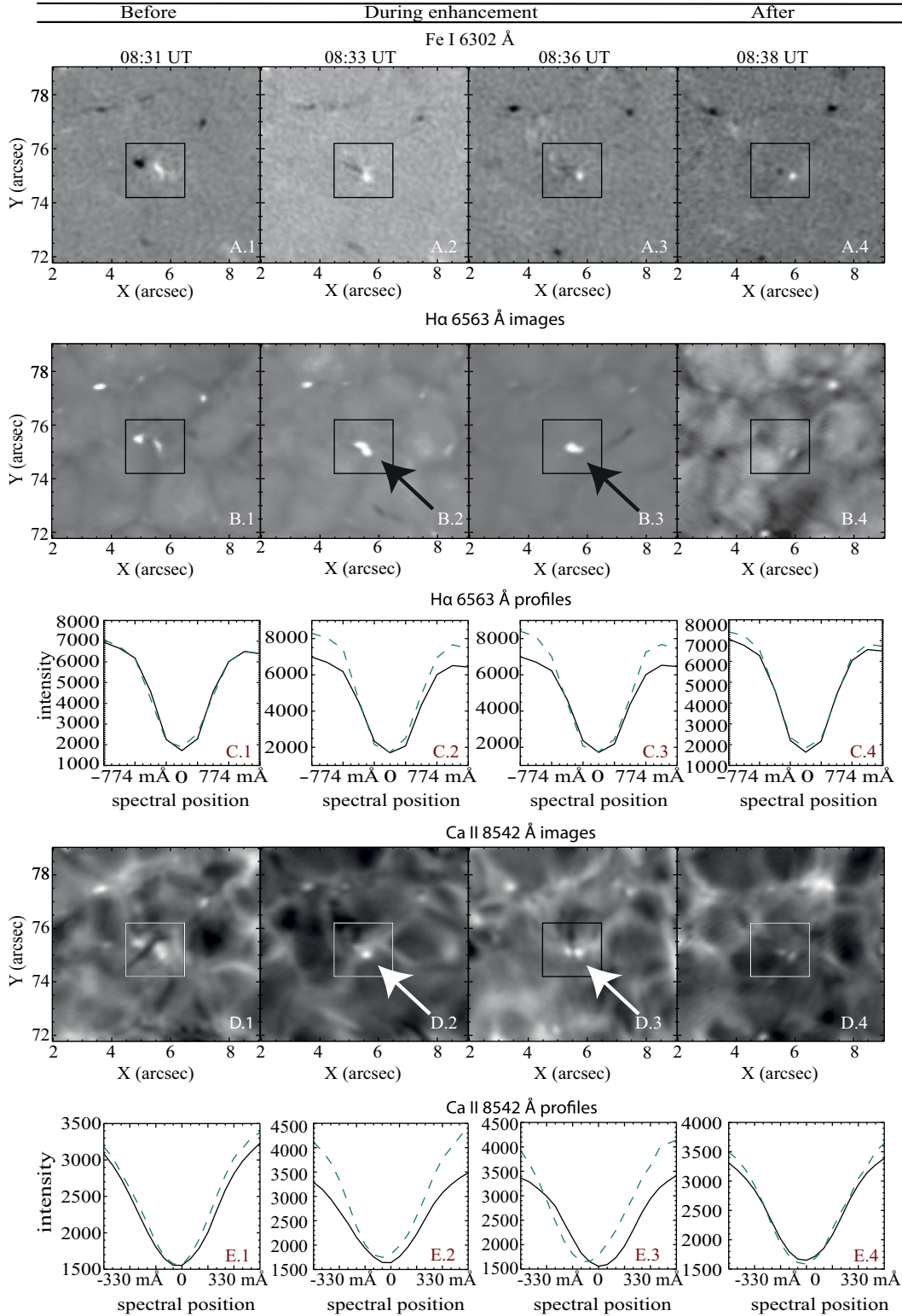
Figure 6. Evolution of the EB represented as Case 2. The top panels A1 and A2 are snapshots of interacting opposite polarities as seen in Fe I 6302 Å. In the middle panels B1 and B2, we see an EB–like formation in the Hα wings −1.29 Å and CaII images at −0.495 Å(D1 and D2). The locations of intensity enhancements are indicated by arrows. The line profiles in Hα are shown in panels C1–C4 and CaII line profiles are shown in E1 and E2. The green dashed lines represent the event, and the averaged background line profile is represented by the solid black lines.

Fig. 10 shows one such evolution for magnetic field concentrations at the approximate height of the photosphere and is represented by panels A1–A4. Here, we see two MCs of opposite polarities in-

teracting with each other. The timestamps are separated by 50 s. Approximately 150 s into the simulation, one of the polarities cancels out. This is similar to what we observe in FeI 6302 Å for
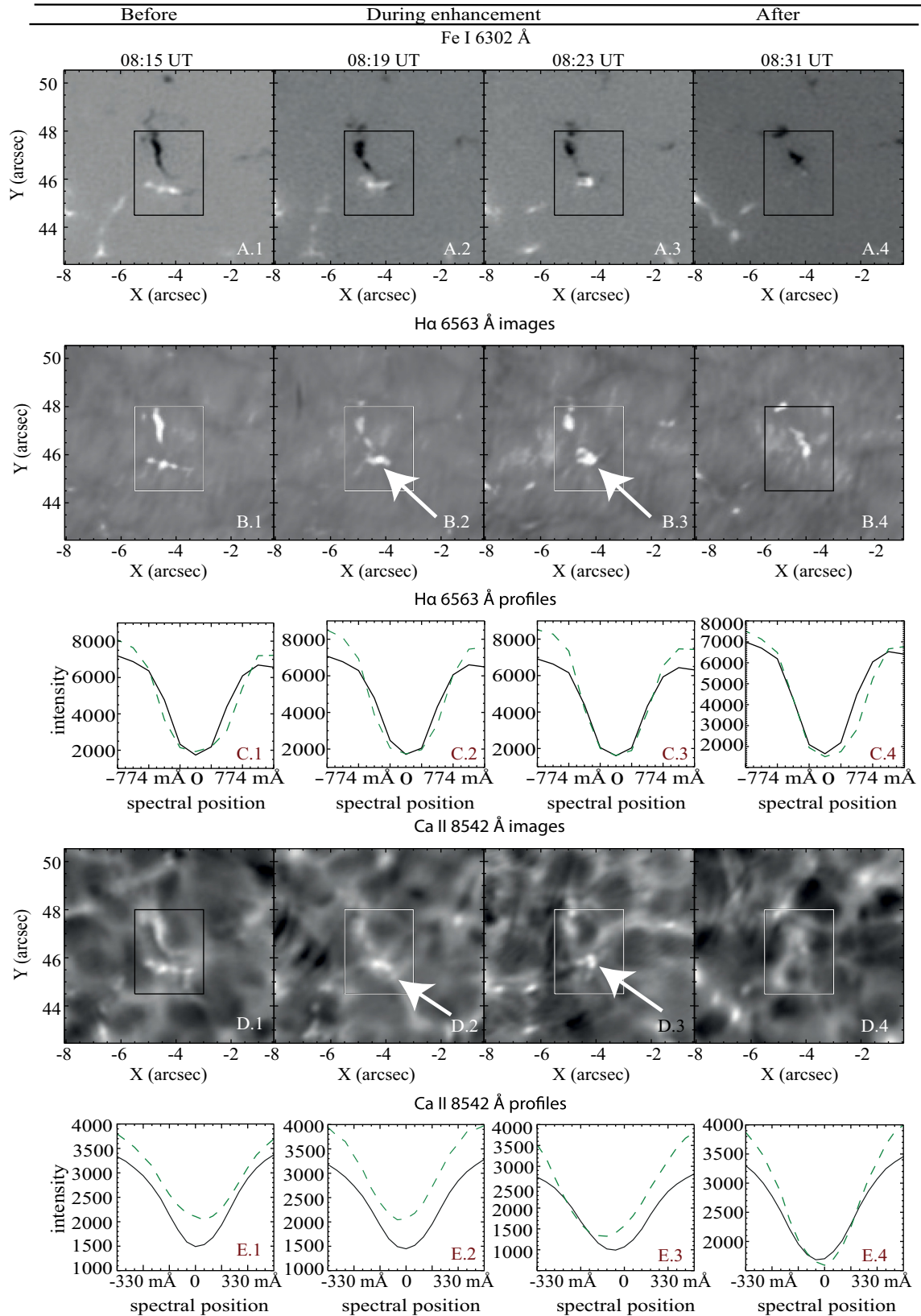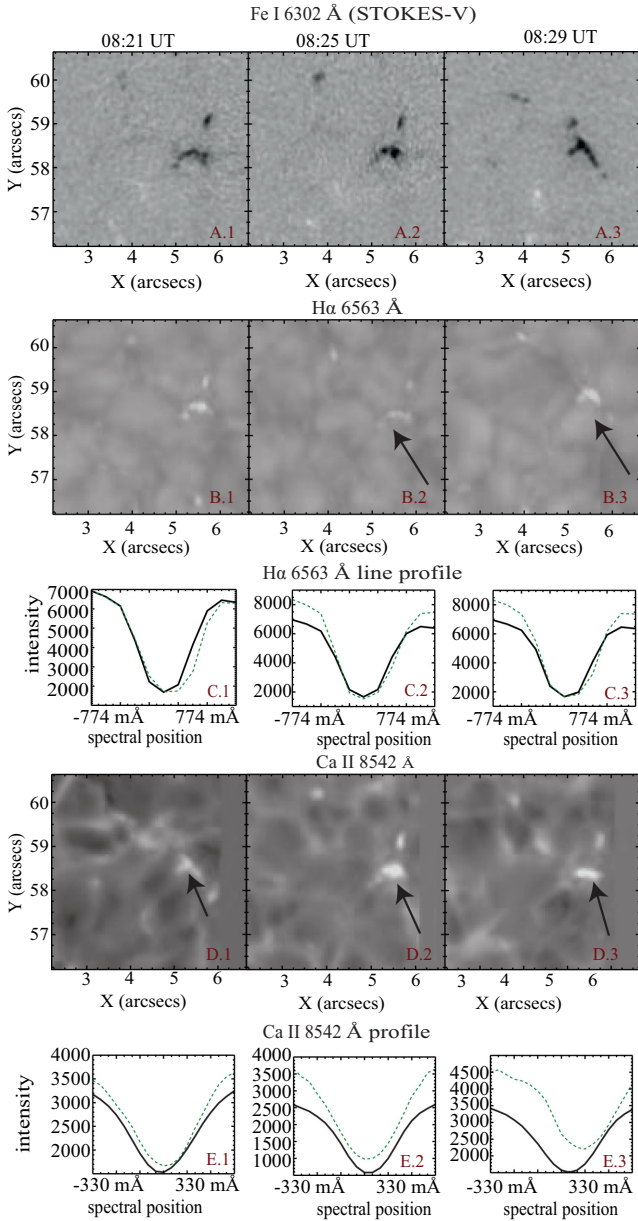
Figure 7. Evolution of the EB represented as Case 3. The top panels A1 and A2 are snapshots of interacting opposite polarities as seen in Fe I 6302 Å. In the middle panels B1 and B2, we see an EB-like formation in the Hα wings −1.29 Å and Ca II images at −0.495 Å(D1 and D2). The locations of intensity enhancements are indicated by arrows. The line profiles in Hα are shown in panels C1–C4 and Ca II line profiles are shown in E1–E2. The green dashed lines represent the event, and the averaged background line profile is represented by the solid black lines.

Fe I 6302 Å (STOKES-V)

08:21 UT   08:25 UT   08:29 UT

Hα 6563 Å

Hα 6563 Å line profile

Ca II 8542 Å

Ca II 8542 Å profile

Figure 8. Top panels show a unipolar event with dominant negative polarity (indicated by 'A' in Fig. 2). The top panels A1 and A2 represent snapshots of interacting opposite polarities as seen in Fe I 6302 Å. In the middle panel (B1 and B2), we see an EB-like formation in the Hα wings −1.29 Å and Ca II images at −0.495 Å(D1 and D2). The locations of intensity enhancements are indicated by arrows. The line profiles in Hα are shown in panels C1–C4, and Ca II line profiles are shown in panels E1 and E2. The green dashed lines represent the event, and the averaged background line profile is represented by the solid black lines.

all events (see panels A1–A4 of Figs 6 and 7). The corresponding magnetic field cancellation rate at the photosphere and at the level 430 km above the photosphere is shown in Fig. 11. Here, the left-hand panel corresponds to the panels A1–A4 of Fig. 10. These magnetic flux curves are plotted by summing the magnetic flux in the opposite polarities, as the polarities evolve in time.

Furthermore, the intergranular magnetic field concentrations expand into the higher layers of the simulated solar atmosphere due to a magnetic–thermal pressure balance, and thermal pressure de-
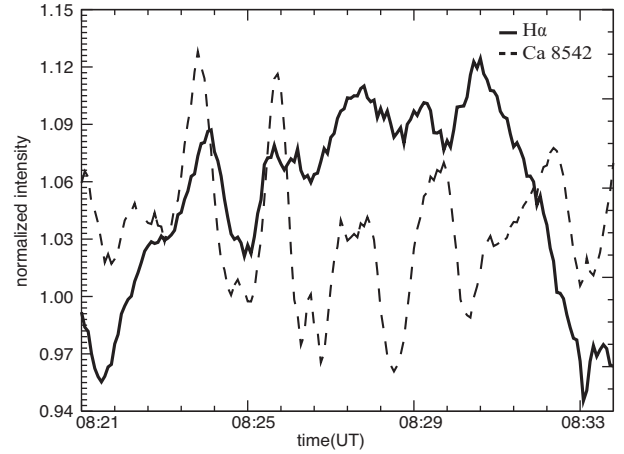

Figure 9. The light curves for unipolar region shown in Fig. 8. The light curves in Hα (solid black) wings at ± 1.29 Å and Ca II 8542 Å (black dashed) wings at ± 0.495 Å.

creases with height. Such evolution of intergranular magnetic field concentrations is shown in panels B1–B4 of Fig. 10. These timestamps are taken at 430 km above the photosphere and are separated by 50 s. The right-hand panel of Fig. 11 shows a magnetic flux cancellation rate at this level.

Due to the geometry of the magnetic field in the simulations, it is expected that the reconnection process evolves in time from the top of the simulation domain towards the solar interior, with the reconnection point moving downwards. This instant of reconnection is seen as an enhancement in the simulations. Fig. 12 shows temperature maps taken at the continuum level and lower chromosphere/upper photosphere (∼430 km above the photosphere). Each panel is separated by 50s. The red arrows show the locations that indicate heating (dark/black colour). Here, we see that the temperature rise occurs in panel B1 and continues throughout the evolution. However, in the panels representing the photosphere, the enhancement here is relatively small and appears ∼100s later. Such behaviour matches with the observations. The temperature curves are plotted in Fig. 13, the solid red line corresponds to the photospheric continuum level, while the solid black line corresponds to the lower chromospheric (upper photospheric) level. The temperature peaks at ∼250s at 430 km at upper photospheric level and at ∼350s for the photosphere.

The time for the reconnection point to move downwards can be estimated by a similar method described in Keys et al. (2013). Here, the authors calculate a velocity of 1.8 km s^{-1} for bright-point motions. The mean horizontal speed in the photosphere in the reconnection region, as the simulations show, is ∼4 km s^{-1} (2 × 1.8 km s^{-1}). For the sake of simplicity, it can be assumed that the reconnecting magnetic field concentrations move towards each other with this speed. The expansion factor of the intergranular magnetic flux tubes is about 2km between the continuum formation layer and the layer 600 km above it, and the magnetic field concentration size at the photospheric layer is about 200km. Assuming straight field lines, the fields from two flux concentrations touch at +600km when there is a 2km gap between them at the continuum formation layer. It takes about 50s for the flux concentrations to touch at the continuum formation layer during that time the contact point above has moved down by 600km. Therefore, the time for the reconnection point to move, from the +600km layer down to the continuum formation layer is also about 50s. The same calculations work if it takes 100s
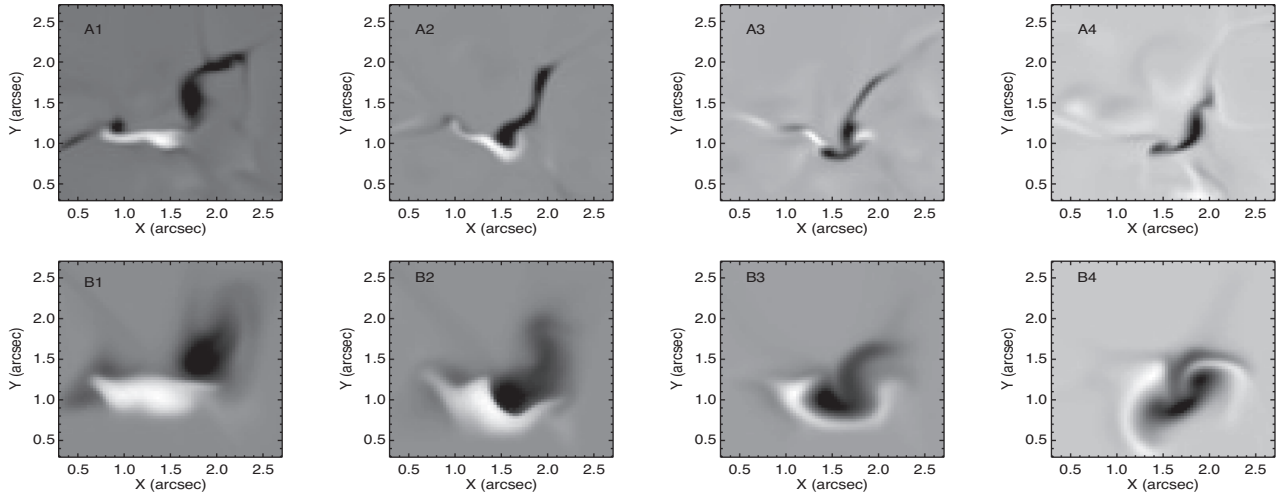
Figure 10. Evolution of magnetic field concentrations in the MURaM simulations. The timestamps are separated by 50s. The top row with panels A1–A4 shows interacting opposite polarity MCs at the photospheric levels. The bottom row with panels B1–B2, show the responses of the interactions to MCs at ∼430 km above the photosphere.
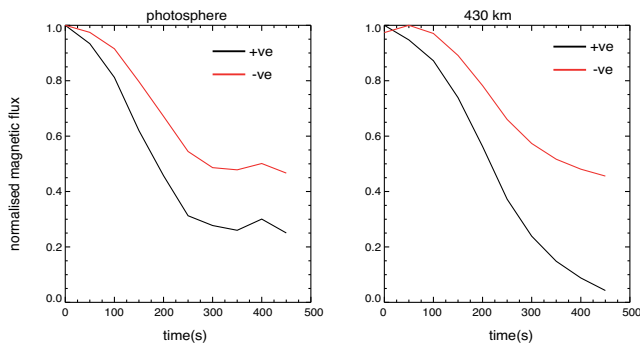

Figure 11. The rate of change in magnetic flux at Fe I 6302 Å as simulated in the MURaM simulations for the regions represented in Fig. 10. The left-hand panel shows the rate of change in magnetic flux at the photospheric continuum level, and the right-hand panel shows rate of change in magnetic flux at 430 km above the photosphere.

to move from the upper photosphere to the continuum layer. The calculation depends on the relative motion speed of the opposite polarity magnetic field concentrations given in Fig. 13. A simple model for this calculation is sketched in the diagram in Fig. 14.

This is a simplistic calculation, and it does not represent the whole complexity of the dynamic process occurring in the simulation domain. However, it gives us a clue of the scale of the reconnection time-scales, and consequently the delay between the upper photospheric and lower chromospheric signals in the Stokes-I profiles of the corresponding absorption lines (e.g. Hα 6563 Å and CaII 8542 Å).

6 DISCUSSIONS AND SUMMARY

We use observations from Hα, CaII 8542 Å, and Fe I 6302 Å spectral lines to investigate the lower solar atmosphere. In FeI 6302 Å (−40mÅ), we observe the Stokes-V signal that is similar to a magnetogram. We observed several events that gave rise to impulsive, flare-like enhancements in the wings of Hα and CaII 8542 Å. These events are associated with the interaction of opposite polarities in

Stokes-V of Fe I 6302 Å. The aim of the paper is to show that QSEBs are observed as low-intensity contrast events. Fig. 2 shows our selected events corresponding to a reduction in the Stokes-V intensity accompanied by a maximum Hα wing intensity. The peak in the Hα wing intensity is ≈20 per cent above the average background or less. When compared to the other events in the detection algorithm these events stand out. Thus, we have presented QSEBs with less than 20 per cent intensity increase that satisfies various cancellation models discussed by Georgoulis et al. (2002) and have all the signatures of EBs found in an active region. However, they show a low-intensity impulsive nature (see panels C1–C4 of Figs 6 and 7). We have used MURaM simulations to understand these events. The sudden enhancement in the wings of the Hα line and CaII line profiles suggest a physical nature similar to that of EBs. We propose that the reason for the low-intensity contrast of QSEB compared to active region EBs is due to the weaker flux cancellation, and the subsequent energy transferred to radiative energy is lower than in regular active region EBs. EBs present near a sunspot have a characteristic recurrent flame-like emission, which recurs with simultaneous Hα and CaII 8542 Å wing enhancements. We see such recurring emissions in QSEBs that have a well-defined EB-like morphology (see Fig. 7). In addition to the Hα signatures, we see an increase in both the core and the wings of the CaII line profile. Ca II profiles associated with the QSEBs are also asymmetrical compared to the Hα profile.

Another aspect of our observations is the presence of a temperature increase corresponding to the QSEBs. This temperature increase is especially seen in Ca II 8542 Å wing emissions. The light curves (see Figs 4 and 5) show that in most of the cases we see CaII 8542 Å wing emissions occurring before the Hα wing emissions. The temperature increase further indicates that the increase in emission intensity occurs higher in the upper photosphere, and the effects propagate downwards. Such morphology is also observed in the MURAM simulations (see Figs 12 and 13). Here, we see that the temperature increase occurs higher in the atmospheric layer (at 7000 K or 430km above the photospheric continuum) and occurs before a temperature rise in the photospheric continuum level. This model is further supported by the fact that the SDO channels formed at the continuum level show intensity peaks after the
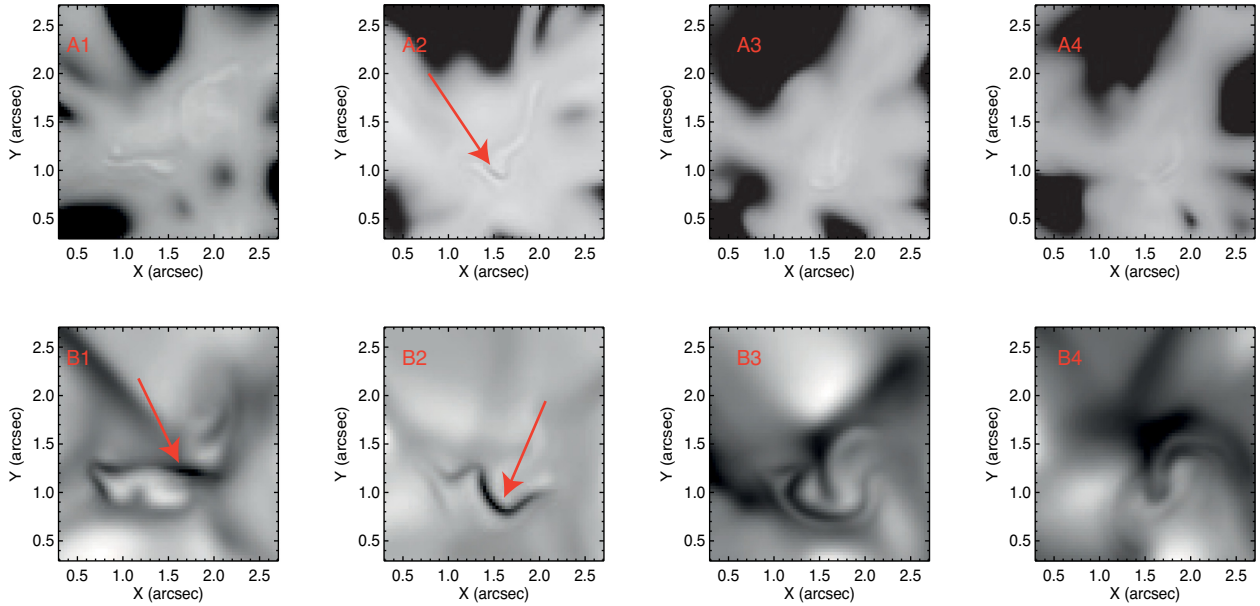
Figure 12. Evolution of temperature, corresponding to panels in Fig. 10 from the MURaM simulations. The timestamps are separated by 50 s. The top row with panels A1–A4 shows temperature change at the photospheric level. The bottom row with panels B1 and B2 shows the temperature change at ∼430 km above the photosphere.
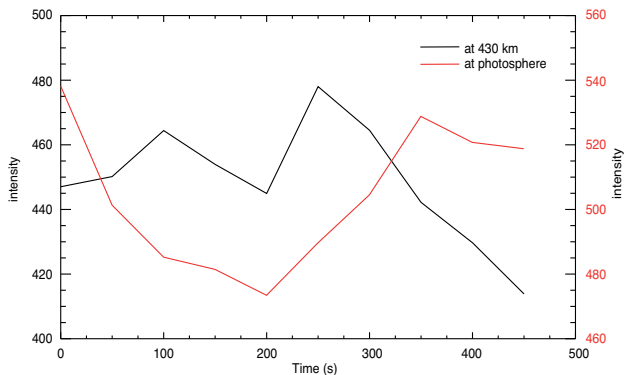

Figure 13. Evolution of intensity, corresponding to panels in Fig. 10 from the MURaM simulations. The timestamps are separated by 50s. The top row with the panels A1–A4, shows temperature change at photospheric levels. The bottom row with panels B1–B2, shows the temperature change at 430 km above the photosphere.
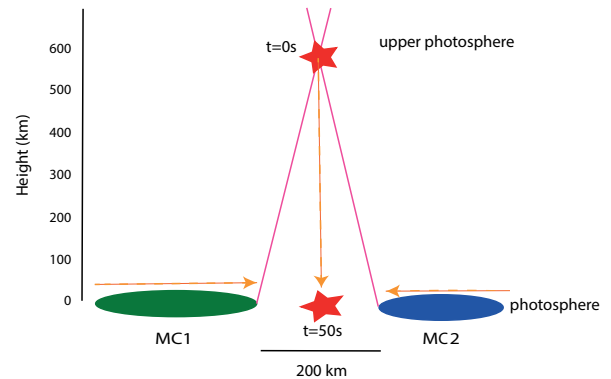

Figure 14. Simple cartoon explaining the observed and simulated scenario. Here, we see two MCs separated by 200 km. The arrows indicate the direction of apparent motion. The pink solid lines show the possible straight magnetic field lines. The stars indicate two flaring regions. The flaring at 600 km (upper photosphere) occurs 50s before the flaring at the continuum level. The image is not scaled.

intensity peaks observed in the chromospheric lines of Hα and Ca II 8542 Å.

Furthermore, our simulations indicate that only a small temperature increase in the lower photosphere is required to reproduce the observed line profiles. This temperature change occurs at the continuum layer 480 km above the assumed photosphere (see Fig. 13). These simulations give us a clue of the scale of the reconnection time-scales, and consequently the delay between the upper photospheric and lower chromospheric signals in the Stokes-I profiles of the corresponding absorption lines (e.g. Hα 6563 Å and Ca II 8542 Å).

REFERENCE

Berger T. E. et al., 2004, A&A, 428, 613

Danilovic S., 2017, A&A, 601, A122

Ellerman F., 1917, ApJ, 46, 298

Fang C., Tang Y. H., Xu Z., Ding M. D., Chen P. F., 2006, ApJ, 643, 1325

Georgoulis M. K., Rust D. M., Bernasconi P. N., Schmieder B., 2002, ApJ, 575, 506

Hagenaar H. J., Shine R. A., 2005, ApJ, 635, 659

Hansteen V. H., Archontis V., Pereira T. M. D., Carlsson M., Rouppe van der Voort L., Leenaarts J., 2017, ApJ, 839, 22

Harvey K., Harvey J., 1973, Sol. Phys., 28, 61

Isobe H., Tripathi D., Asai A., Jain R., 2007, Sol. Phys., 246, 89

Keys P. H., Mathioudakis M., Jess D. B., 2013, MNRAS, 428, 3220

Leenaarts J., Carlsson M., Hansteen V., Rouppe van der Voort L., 2009, ApJ, 694, L128

Leenaarts J., Carlsson M., Rouppe van der Voort L., 2012, ApJ, 749, 136

Leenaarts J., Rutten R. J., Carlsson M., Uitenbroek H., 2006, A&A, 452, L15

Leenaarts J., Rutten R. J., Sütterlin P., Carlsson M., Uitenbroek H., 2006, A&A, 449, 1209

Lemen J. R. et al., 2012, Sol. Phys., 275, 17

Livingston W., Wallace L., 1987, ApJ, 314, 808

McMath R. R., Mohler O. C., Dodson H. W., 1960, Proc. Natl. Acad. Sci., 46, 165

Muller R., Mena B., 1987, Sol Phys., 112, 295

Nelson C. J., Doyle J. G., Erdélyi R., Huang Z., Madjarska M. S., Mathioudakis M., Mumford S. J., Reardon K., 2013, Sol. Phys., 283, 307

Nelson C. J., Freij N., Reid A., Oliver R., Mathioudakis M., Erdélyi R., 2017, ApJ, 845, 16

Nelson C. J., Scullion E. M., Doyle J. G., Freij N., Erdélyi R., 2015, ApJ, 798, 19

Nelson C. J., Shelyag S., Mathioudakis M., Doyle J. G., Madjarska M. S., Uitenbroek H., Erdélyi R., 2013, ApJ, 779, 125

Pariat E., Schmieder B., Berlicki A., Deng Y., Mein N., López Ariste A., Wang S., 2007, ApJ, 473, 279

Pesnell W. D., Thompson B. J., Chamberlin P. C., 2012, Sol. Phys., 275, 3

Peter H. et al., 2014, Science, 346, 1255726

Qiu J., Ding M. D., Wang H., Denker C., Goode P. R., 2000, ApJL, 544, L157

Reid A., Henriques V., Mathioudakis M., Doyle J. G., Ray T., 2017, ApJ, 845, 100

Reid A., Mathioudakis M., Doyle J. G., Scullion E., Nelson C. J., Henriques V., Ray T., 2016, ApJ, 823, 110

Reid A., Mathioudakis M., Scullion E. M., Doyle J. G., Shelyag S., Gallagher P., 2015, ApJ, 805, 64

Rouppe van der Voort L. H. M., Hansteen V. H., Carlsson M., Fossum A., Marthinussen E., van Noort M. J., Berger T. E., 2005, ApJ, 435, 327

Rouppe van der Voort L., Rutten R. J., Vissers G. J. M., 2016, A&A, 592, A100

Rutten R. J., Vissers G. J. M., Rouppe van der Voort L., Sütterlin P., Vitas N., 2013, Journal of Physics Conference Series, 440, 012007

Scharmer G. B., Bjelksjo K., Korhonen T. K., Lindberg B., Petterson B., 2003, Proc. SPIE, 4853, 341

Scharmer G. B. et al., 2008, ApJ, 689, L69

Severny A. B., 1956, The Observatory, 76, 241

Sheeley N. R., Jr, 1969, Sol Phys., 9, 347

Spruit H. C., 1976, Sol Phys., 50, 269

Tian H., Xu Z., He J., Madsen C., 2016, ApJ, 824, 96

Title A. M., Berger T. E., 1996, ApJ, 463, 797

van Noort M., Rouppe van der Voort L., Löfdahl M. G., 2005, Sol Phys., 228, 191

Vissers G. J. M., Rouppe van der Voort L., Rutten R., 2013, ApJ, 74, 13

Vissers G. J. M., Rouppe van der Voort L., Rutten R. J., Carlsson M., De Pontieu B., 2015, ApJ, 812, 11

Vrabec D., 1971, Sol. Magn. Fields, 43, 329

Vögler A., Shelyag S., Schüssler M., Cattaneo F., Emonet T., Linde T., 2005, A&A, 429, 334

Watanabe H. et al., 2008, ApJ, 684, 736

Watanabe H., Vissers G. J. M., Kitai R., Rouppe van der Voort L., Rutten R. J., 2011, ApJ, 736, 71

Zachariadis T. G., Alissandrakis C. E., Banos G., 1987, Sol. Phys., 108, 227

This paper has been typeset from a TeX/LaTeX file prepared by the author.